ORIGINALS

Ch. Brücker · J. Spatz · W. Schröder

Feasability study of wall shear stress imaging using microstructured surfaces with flexible micropillars

Abstract A new optical sensor technique based on a sensor film with arrays of hair-like flexible micropillars on the surface is presented to measure the temporal and spatial wall shear stress field in boundary layer flows. The sensor principle uses the pillar tip deflection in the viscous sublayer as a direct measure of the wall shear stress. The pillar images are recorded simultaneously as a grid of small bright spots by high-speed imaging of the illuminated sensor film. Two different ways of illumination were tested, one of which uses the fact that the transparent pillars act as optical microfibres, which guide the light to the pillar tips. The other method uses pillar tips which were reflective coated. The tip displacement field of the pillars is measured by image processing with subpixel accuracy. With a typical displacement resolution on the order of 0.2 μm, the minimum resolvable wall friction value is $\tau_w \approx 20$ mPa. With smaller pillar structures than those used in this study, one can expect even smaller resolution limits.

1 Introduction

One of the still unsolved challenging tasks in experimental fluid mechanics is the measurement of the wall shear stress distribution on surfaces with high temporal and spatial resolution. This is due to the small forces per unit area acting along the local surface element, which requires a high resolution and signal-to-noise ratio of the

C. Brücker (✉) · W. Schröder
Aerodynamisches Institut der RWTH Aachen,
Wüllnerstr. 5-7, 52062 Aachen, Germany
E-mail: bruecker@aia.rwth-aachen.de
Tel.: +49-241-8095429
Fax: +49-241-8092257

J. Spatz
Physikalisch-Chemisches Institut, Universität Heidelberg,
INF 253, 69120 Heidelberg, Germany

sensor. While single-point sensors with various operating principles have been successfully applied to simple canonical flows like, e.g. the flow over a flat plate, there is still a lack of an appropriate quantitative imaging technique to resolve the fluctuating wall shear stress field over an entire surface of interest, such as that induced by coherent structures in turbulent flows. Such measurements with high temporal and spatial resolution are of fundamental interest since they deliver the necessary information for any implementation of active control of wall-bounded flows.

In the last decade microfabrication has reached a production level to scale down measurement devices such that they can be applied in the very near wall region without disturbing the outer flow. Classical measurement techniques like hot-wire anemometry and laser Doppler anemometry have been miniaturised to measure the velocity gradient in the viscous sublayer and to determine the wall shear (Sturzebecher et al. 2001; Czarske et al. 2001; Khoo and Durst 2002; Gharib et al. 2002; Gibson et al. 2004). However, these techniques measure only at one single measurement location. In contrast, optical techniques, like, e.g. oil film interferometry, provide a surface profile of the wall shear distribution, but only in quasi-steady flow. An overview of the different techniques and their limitations is given in the review papers by Fernholz et al. (1996), Löfdahl and Gad-el-Hak (1999) and Naughton and Sheplak (2002).

Measurement principles based on microfences or wind hairs have become more attractive because of the progress in the fabrication of arrays of microsensors to achieve a sufficient resolution. Such an approach has been presented by van Baar et al. (2003), who designed an artificial wind hair device with a stiff cantilever, which is fixed on a spiral spring suspension. A capacitive read-out principle is proposed and first prototypes are currently being fabricated. Similar approaches to design artificial wind hairs were published earlier by Osaki et al. (2000) and by the group of Chen et al. (2003). The sensory hair in Osaki's prototype was about 1,500-μm-long, with a single hair on one chip. The

angular deflection is transformed into a measurement value using strain gauges fabricated at the bottom of the hair. Chen et al. (2003) used a platelet with a size of 180×1,100 μm, which is flapped from the base into the flow and the drag is measured with a strain gauge at the base also. A similar sensor principle is used by von Papen et al. (2002) to measure the wall shear stress fluctuations at a single point with frequencies of up to 1 kHz. The microelectromechanical systems (MEMS) surface fence sensor consists of a 5-mm-long, 100–300-μm-high and 7–10-μm-thick silicon fence. The drag-induced deflection is being transformed into an electrical signal, which is proportional to the component of the wall shear stress perpendicular to the fence. Since all these methods use an electronic read-out principle at the bottom of the sensors, which needs some space to integrate the electronics, the size and spacing of the sensor elements are usually large compared to the micropillar arrays presented in this study. Furthermore, these devices are critical with respect to contamination, fouling and eventual cracking. In addition, the rigidity of the sensor restricts the application to only planar surfaces.

Since the development of atomic force microscopy, force measurement techniques using microscopic cantilever beams are increasingly applied in biology. Arrays of micropillars made of silicon were recently used by one group of the authors to study bio-functional filament systems in which the filaments are bonded at the pillar tips in a well defined arrangement (Fig. 1a in Roos et al. 2003). This method offers a new area of biological experiments, since the access is not impeded by surfaces (Roy et al. 2002; Weeks et al. 2003). The sensor concept presented in this paper is based on the same principle by fabricating a film-type sensor with a dense array of flexible micropillars. Micropillars with diameters of a few microns are manufactured from elastomers, which have high flexural and tensile yield strength values, e.g. polydimethylsiloxane (PDMS); as such they are very flexible and easily deflected by the fluid forces. When such a surface sensor is placed in a boundary layer flow, the pillars are bent until the equilibrium of the drag force

and the internal elastic strain. Because of their micro size, their tips lie almost completely within the viscous sublayer, which results in a tip displacement directly proportional to the wall shear stress. The flexible sensor film with the micropillars can be used also on curved surfaces and under severe environmental condition, since PDMS has unique chemical and physical attributes, such as a low glass transition temperature (TG −125°C), a unique flexibility (the shear modulus G may vary in the range 0.1–3 MPa), usability over a wide temperature range (at least from −100°C up to +100°C) and a very high notch impact strength (Lötters et al. 1997). In addition, the transparency of PDMS lets the pillars act like optical microfibres. This fact is useful for efficient optical detection of the pillar bending in magnitude and in direction (Brücker et al. 2004). For aerodynamic applications, the concept of a sensor film with flexible micropillars made from PDMS enables time-resolved wall shear stress measurements over larger areas within a dense array of sensor elements, which can be detected simultaneously by optical high-speed imaging. In brief, these attributes give the new sensor concept a unique potential in experimental aerodynamics.

2 Fabrication of the sensor

The micropillars were fabricated by the moulding of the transparent elastomer PDMS (Sylgard 184 Dow Chemical) using negative-image masters with holes patterned by photolithography. To achieve a high aspect ratio AR of the micropillars, which has an important influence on the sensitivity of the sensor elements as shown in Sect. 3.2, masters with different thicknesses of between 30 μm and 100 μm were used. The silicone mixture in a ratio of 10:1 (rubber base/cure) was outgassed in a vacuum for 30 min before applying to the master and was cured at room temperature for 3 days. The Young's modulus under this condition is approximately $E \approx 0.75$ MPa. Thereafter, the sensor film is peeled off carefully to prevent plastic deformation or rupture of the pillars during the de-moulding process due to the friction forces acting on the pillars. The Raster Electron Microscopy (REM) picture in Fig. 1a demonstrates that micropillars with an approximately cylindrical shape at a diameter of $D \approx 8$ μm and an aspect ratio of about $L/D \approx 8$ could be manufactured.

Fig. 1 Raster Electron Microscopy (REM) image of the sensor film with microfabricated micropillars for wall shear stress imaging. Sensor type "A" (*left*); substrate: PDMS, manufacturing technique: negative photoresist and casting. Sensor type "B" (*right*); substrate: PDMS, manufacturing technique: laser drilling in wax film and casting
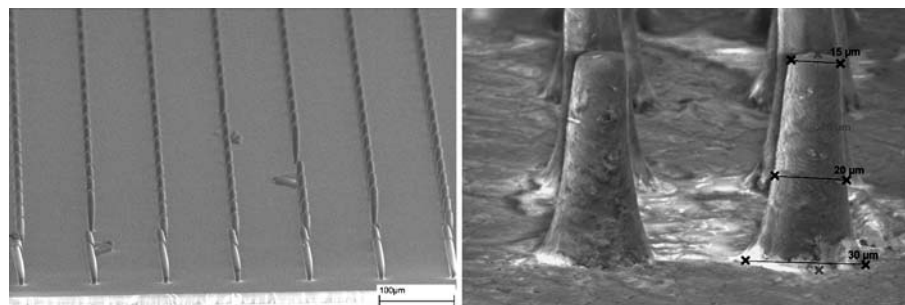
Fabrication tests with the different masters showed that this is the maximum aspect ratio of the pillars at this diameter for which the peel-off can be handled without damage to the pillars. The micropillars were arranged in a 2D array with an equidistant spacing of about 95 μm and the overall sensor area is 2 cm × 2 cm. Finally, the pillars are sputtered with gold to enhance the reflectivity on their tips. Sensor films with such kind of micropillars are referred to in the following as type "A."

Recently, we developed an alternative fabrication technique with the potential to achieve a higher aspect ratio of the micropillars (Schmitz et al. 2005). A thin planar wax film is used in which small bores are drilled with an excimer laser. Thereafter, the PDMS is cast into the bores under a vacuum. After curing, the wax is melted with hot de-ionised water and washed out. Note that the peel-off problem does not exist any more, which, in principle, allows to cast pillars with higher aspect ratios. The first sensor prototype based on this fabrication technique is shown in Fig. 1b. The pillars have the shape of semi-hyperboloids, which is a result of the production process. The rounded tip is formed as a consequence of the capillary forces and can be controlled by the filling pressure. When illuminated from the back plane, the specific semi-hyperbolic form of the transparent pillars at the foot acts as a light collimator, which leads to a bright spot at the pillar tip. Most of the pillars are well formed with a surface roughness in the nanoscale regime. As demonstrated recently, we could achieve pillars with a diameter of $D{\approx}15$ μm and a maximum aspect ratio of about $L/D{\approx}25$. Sensor films with such kind of micropillars are referred to in the following as type "B."

3 Sensor sensitivity and response

The sensor principle uses the pillar tip deflection in the viscous sublayer of turbulent boundary layer flows as a measure that is directly proportional to the wall shear stress. This assumption is justified, as shown later in Sect. 3.2, since the velocity profile is linear and the drag of the micropillar is dominated by the viscous Stokes' drag. The pillar length L is, therefore, restricted to a maximum of a few viscous wall units such that the tip lies almost within the viscous sublayer. In turbulent flows, a high sensitivity is necessary to determine the temporal wall shear field with a sufficiently high resolution, since the fluctuating wall shear values may extend up to 40% of the mean wall shear. As shown in the subsequent sections, the resolution depends mainly on the diameter and aspect ratio of the pillars, and is limited by the technological constraints of the microfabrication process and the Young's modulus E of the material. In the following, the pillar is considered in a first approximation as a uniform and homogeneous slender cylindrical beam. The coordinate system is depicted in Fig. 2. Note that, like in cantilever mechanics, the z axis
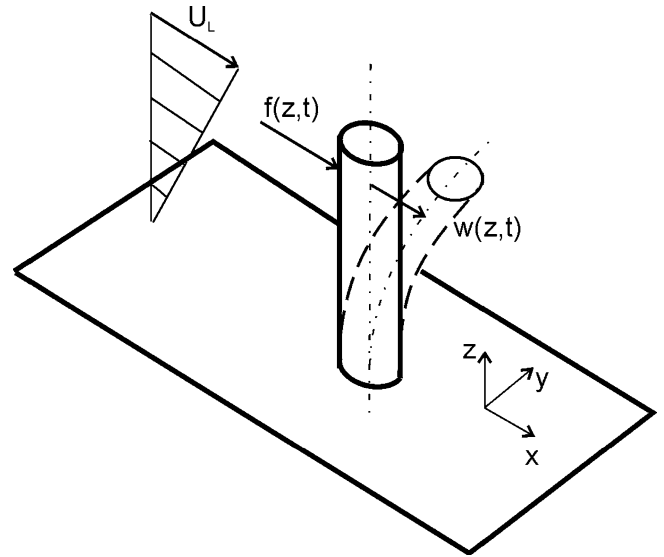

Fig. 2 Definition of the coordinate system

denotes the wall-normal coordinate along the straight pillar axis in the unforced situation.

3.1 Load profile along the pillar axis

With a typical length $L{\approx}60\text{–}80$ μm as shown in Fig. 1, the tips of the micropillars almost lie within the viscous sublayer up to a normalised thickness of approximately $5z+$ (where $z+$ is the characteristic wall unit) for most of the practical turbulent flow situations. According to the definition of a hydraulically smooth wall, the pillars do not disturb the global flow under these constraints. Following Bernard and Wallace (2002), the velocity distribution near the wall in turbulent flows can be approximated by a linear profile up to a normalised wall distance of $5z^+$. The Taylor expansion for U^+ and u_{rms}^+ reads:

$$\bar{U}^+(z^+) = z^+ - \frac{(z^+)^2}{2\,Re_{\,\tau}} + \dots \tag{1}$$

$$\frac{u_{\mathrm{rms}}^+}{\bar{U}^+} = 0.4 + z^+\left(\frac{0.2}{Re_{\,\tau}} + 0.07\right) + \dots \tag{2}$$

The second terms on the right hand side of the equations and higher order terms vanish for typical turbulent Reynolds numbers $Re_\tau > 150$, defined by the friction velocity u_τ. The Reynolds number at the pillar tip $Re = \eta U_L D/\rho$, based on the tip velocity U_L, is usually on the order of $Re < O(10^{-1})$, due to the microscale of the pillars and the small velocities in the viscous sublayer. Therefore, the drag on the micropillar is approximately linearly proportional to the velocity, as predicted in the Stokes' limit $Re \ll 1$. Hence, the load profile along the pillar axis is linear for a homogeneous cylindrical beam considered to be a first approximation.

3.2 Pillar bending: quasi-steady approximation

In the case of quasi-steady flow around the pillar, the Stokes' solution can be simplified by the Oseen approximation of the drag coefficient, which is valid for a pillar tip Reynolds number up to $Re = O(1)$. Hence, the pillar deflection w_L at the head can be estimated by integrating the drag coefficient along the pillar axis under the assumption of a linear velocity profile. This results in a first approximation of the pillar tip deflection as:

$$\left(\frac{w_L}{L}\right) \approx \frac{11.7\eta\dot{\gamma}}{E\ln(L/2D)}\left(\frac{L}{D}\right)^4 \tag{3}$$

which has been derived by Venier et al. (1994) for the application in a microtubule. The variables herein are the fluid viscosity η, the shear rate at the wall $\dot{\gamma}$ and the Young's modulus E. Note that further assumptions made herein are the validity of the Euler–Bernoulli elastic beam theory, a 2D flow around the pillar, a small tip deflection and no end-wall effects at the pillar base. The equation demonstrates that the pillar deflection at the tip is directly proportional to the product of the shear rate and the viscosity; hence, it is proportional to the wall shear stress. Besides, it shows the deflection to mainly depend on the pillar aspect ratio L/D and the flexibility expressed by Young's modulus. The sensitivity X of the sensor is defined as the ratio of the pillar tip deflection amplitude to the wall shear $X = w_L/\tau_W$. If we assume a technologically achievable aspect ratio in the range of $10 < L/D < 20$, it follows that the sensitivity roughly scales with $X \sim L^{4.5}$.

3.3 Pillar bending: frequency response

The frequency response of the micropillars should be adapted to the typical spectra in turbulent flows. Let us consider a flat plate boundary layer flow at $Re_\theta = 4,000$, in which the Kolmogorov length scale is on the order of 100 μm. The energy spectra show that the energy content above 5–10 kHz is almost negligible (Bernard and Wallace 2002). It is further assumed that only the low-frequency range portion persists within the viscous sublayer, which is associated with the near-wall dynamics of the coherent vortex structures. Therefore, the sensor should resolve at least frequencies in the range between 1 Hz up to a maximum on the order of several 100 Hz. The estimate of the frequency response of the pillars follows the work by Shimozawa et al. (1998) and Rudko (2001), and is derived in Appendices 1 and 2. The pillars are treated in the first approximation as uniform, homogeneous, one-sided clamped circular cantilever beams. Unlike the quasi-steady Oseen approximation, the frequency response is calculated using Stokes' approximation because it describes added mass effects, which are present only in oscillatory flows and, hence, do not appear in Oseen's model.

The equation of motion given in Eq. 16 of Appendix 2 includes the inertia of the beam, the bending force, the oscillating external drag force and the viscous damping. The boundary conditions determine the natural frequencies and mode shapes of the beam. The natural frequency of a one-sided clamped cylinder with a length of L and a diameter of D in a vacuum is:

$$f_0 = \frac{D}{8\pi}\frac{\lambda_1^2}{L^2}\sqrt{\frac{E}{\rho}} \tag{4}$$

with the first eigenvalue $\lambda_1 = 1.875$. Equation 4 yields natural frequencies on the order of 3–4 kHz for the given geometry and properties of the pillars; however, the resonance frequency is decreased due to the added mass effect. This is estimated by calculating, in the Appendix, the pillar response to an oscillating flow in the boundary layer. The results are calculated for pillars with a diameter and length of $(D, L) = (10, 100)$ μm and $(10, 200)$ μm in different fluids (air: $\mu = 1.82 \times 10^{-5}$ N*s/m², $\rho = 1.2$ kg/m³; water: $\mu = 10^{-3}$ N*s/m², $\rho = 1,000$ kg/m³; water–glycerine mixture (50% vol): $\mu = 10^{-2}$ N*s/m², $\rho = 1,200$ kg/m³). Figure 3 shows the sensitivity X in response to the oscillating near wall flow, i.e. of the oscillating wall shear; X is defined as the maximum tip deflection w_L, given by Eqs. 22, 23, 24, 25, 26, 27, 28 and 29, divided by the maximum wall shear τ_W, which is determined from the velocity gradient at the wall.

Since the Stokes' mechanical impedance and phase shift do not depend on the velocity magnitude and the phase, as shown by Eqs. 7, 8, 9 and 10, the sensitivity is only a function of the frequency and the size of the pillars. The resonance frequency decreases with increased viscous damping and density of the fluid. The sensitivity scales with $X \sim L^5$, which is slightly higher than in Oseen's approximation. At excitation frequencies f below resonance, the profiles possess a weak exponential response to the frequency. Typical values of the sensitivity in the low-frequency range $f < 100$ Hz amount to 5 μm/Pa at $(D, L) = (10, 100)$ μm and 150 μm/Pa at $(D, L) = (10, 200)$ μm, which demonstrates the strong influence of the pillar length. Figure 3 shows, in addition, the results of the quasi-steady approximations for comparison.

3.4 Estimate of the flow interference of the pillars

The flow disturbance in the near-wall region due to the presence of the micropillars is estimated from a numerical simulation of the Navier–Stokes equations for a 3D steady viscous flow around a small wall-bounded rigid cylinder of diameter $D = 10$ μm and length $L = 100$ μm in a simple planar shear flow with $\dot{\gamma} = 1,000/s$. The Reynolds number at the pillar tip defined by the undisturbed axial velocity equals $Re = 0.1$ for a water–glycerine mixture with a viscosity of 10 cP. Exemplary results are shown in Fig. 4 in the wall-parallel plane crossing the pillar tip. These findings indicate that the
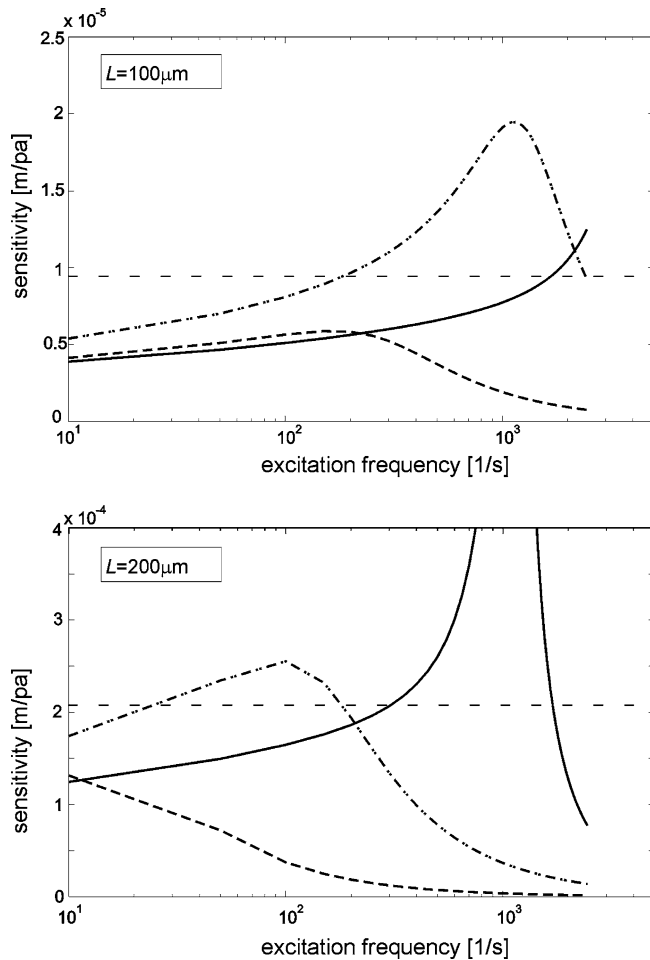
Fig. 3a, b Sensitivity X of the pillars in response to an oscillating boundary layer flow (air *continuous line*; water *dash-dot line*; water–glycerine mixture *dashed line*). **a** $(D, L) = (10, 100)$ μm. **b** $(D, L) = (10, 200)$ μm

flow disturbances decay below 5% of the undisturbed velocity U_L for a radius greater than 100 μm.

3.5 Calibration procedure

Because of possible non-uniformities of the pillars and deviations from the theoretically derived pillar displacement behaviour, the sensor film needs to be calibrated. Therefore, the individual flexural stiffness of each individual pillar is calibrated in a defined shear flow, which is generated in a specially adapted cone-plate-type viscometer, as shown in Fig. 5. The flow in the cone-plate viscometer exhibits a simple planar shear flow with constant shear, similar to flow in the viscous sublayer of a turbulent wall-bounded flow. The sensor is placed flush-mounted with the centre at a radius of 17.5 mm and the pillar tip displacement is measured over a series of different shear velocities and by using different fluids. Figure 6 shows the resulting calibration curve for the pillars of type "A" in water as a carrier medium. The rotation speed of the viscometer was stepwise increased, beginning from 10 rpm up to 1,000 rpm, in increments of 10 rpm in the low-speed range and 20 rpm for the high-speed range. Note that the electronic stabilisation of the stepper motor unit does not allow arbitrary values, but only changes in increments of 10 rpm. Each circle in the plot is an average of 50 samples of a single pillar measurement. The calibration curve shows a well defined linear curve over the main course of wall shear values, while larger deviations are seen for values below 80 mPa and above 1 Pa. The deviation in the lower range is a result of the resolution limit with the given optical setup, which is about 0.15 pixels, corresponding to a pillar tip displacement of 0.15 μm. In the upper range above 1 Pa, the pillar tip displacement exceeds values of more than 6 μm, which is about 10% of the pillar length. These deviations originate from the increased bending of the pillar, which changes the drag coefficient in the upper region near the tip and, therefore, the load profile. In addition, with increased bending the elastic behaviour starts to deviate from that described by the linear elastic theory. These results underline the necessity for careful calibration of the sensor in Couette flow. In addition, in situ calibration is possible in canonical flows using the mean value of wall shear as in a fully developed turbulent channel flow or boundary layer flows. The fabrication process in the case of pillars of type "A" reproduces the pillars with a high homogeneity in shape; therefore, only small deviations of the calibration values were found, with an rms value of less

Fig. 4 Viscous flow around a single rigid pillar at $\text{Re}_D(z = L) = 0.1$. *Left*: contours of the deviation of the axial velocity component from the undisturbed inflow velocity U_L. *Right*: contours of the transversal velocity relative to U_L
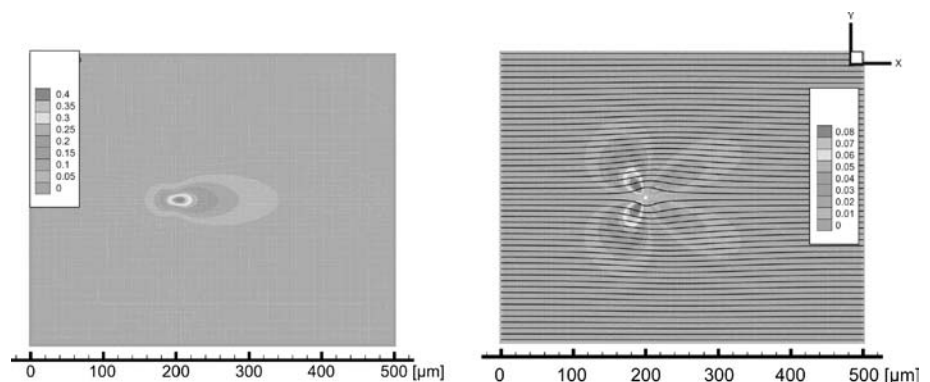
than 3% of the average spring constant. It is important to note that the lower limit of the measurement resolution, as demonstrated in Fig. 6, is largely limited by the achievable pillar aspect ratio. It was only recently that we succeeded in fabricating pillars with aspect ratios as high as $10 < AR < 20$ and diameters of less than 20 μm, for which we could not finish the detailed calibration procedure in the meantime (Schmitz et al. 2005). However, first preliminary results show that resolution limits of less than 10 mPa can be achieved with these pillars of type "B."

### 3.6 Long-term behaviour and robustness

The PDMS elastomer is assumed to be homogeneous and isotropic. However, real elastomers are viscoelastic and, therefore, do not have perfectly linear deformation curves and can display hysteresis and creep. This has been studied by O'Sullivan et al. (2003) for different elastomers. The results demonstrate, for the same family of rubber specimens as PDMS, an initial creep of less than 2.5% in a 1-h period, as predicted by the Zener model, until the rubber has extended to 99.9% of its final value under load. Dynamic load plateau tests revealed that hysteresis levels were always the greatest with 2.5% between upload and unload on the initial cycle, with levels reducing up to the third or forth cycle, after which, the hysteresis tended to saturate. The values of modulus, however, remained unchanged during repeated testing. If the elastomer was allowed to stand unstressed, the hysteresis behaviour described above was recovered. They concluded from their results that force sensors incorporating elastomer springs, similar to micropillars, should be cyclically loaded prior to use to lower overall hysteresis levels and to ensure saturation (constant) values. In our calibration tests, we could not detect any hysteresis effect within the resolution limit.

The critical height L_c for the buckling of the pillars under their own weight can be estimated from the Euler theory for elastic instabilities and can be found in, e.g. Timoshenko and Gere (1961):

$$L_c = \left(\frac{7.837 E D^2}{16 \rho g} \right)^{\frac{1}{3}} \tag{5}$$

For a homogeneous cylindrical pillar made of PDMS with a diameter of $D = 10$ μm, one obtains a theoretical maximum height of $\approx 2,000$ μm, which is far beyond the height of the fabricated pillars. Therefore, no buckling problem exists and the pillars always bounce back to their initial straight form at rest and in an unforced situation with an angle of $\pi/2$ to the sensor backing. Another common problem of small filiform structures in arrays is their tendency of lateral collapse, which is the connection of neighbouring elements through the influence of surface forces. This problem was studied in detail by Glassmaker et al. (2004) for fibrillar surfaces made from PDMS. Once brought together, pillars tend to remain connected due to the adhesion forces, which can be prevented when the separation between the pillars is large enough. As already concluded in Sect. 3.3, the separation between the pillars should be on the order of their height L to prevent flow interference, which also prevents the lateral collapse. Additionally, the pillars have a circular shape, hence, the reduced contact area lowers the risk of lateral collapse.
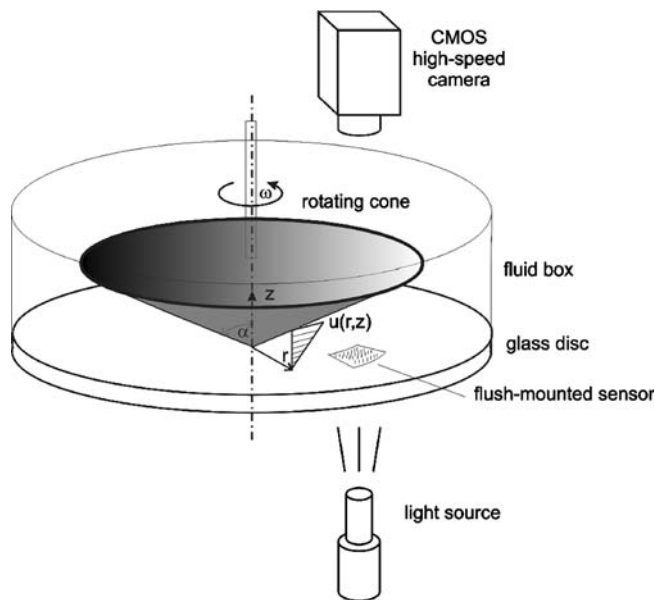
Fig. 5 Calibration procedure of the sensor film with the micropillars in a defined shear flow; the cone and plate are both transparent so as to have complete optical access of the sensor
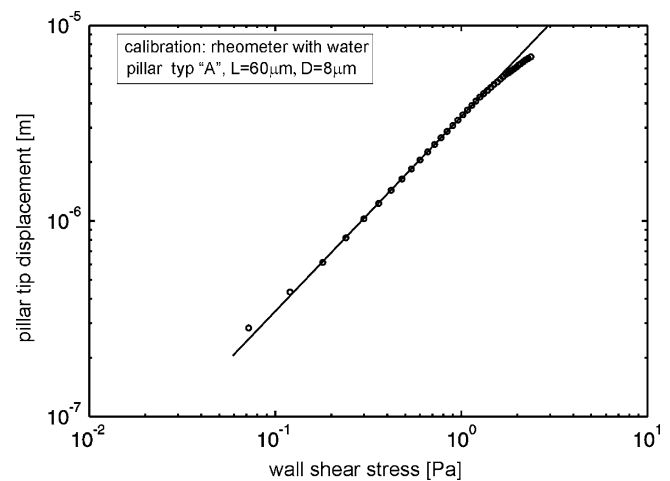
Fig. 6 Sensor calibration curve for the pillars of type "A." The calibration was obtained in the water-filled rheometer with stepwise increase of the rotation speed beginning from 10 rpm to 1,000 rpm in increments of 10 rpm in the low-speed range and 20 rpm for the high-speed range (*circles*: average of 50 samples for a single pillar; *solid line*: linear regression of the inner range)

4 Experiments

4.1 Experimental test conditions

The first proof of principle and tests of the fabricated sensor films were carried out at varying Reynolds numbers in a specially designed transparent flow channel for different fluids, i.e. for deionised water, a water–glycerine mixture at 50% vol with a viscosity of 10 cP and a refractive index of $n = 1.43$ and coal oil with a viscosity of 36 cP and a refractive index of $n = 1.45$. The flow channel has a quadratic cross section ($H = 50$ mm) and a length of 2 m (Fig. 7). The sensor itself is flush-mounted on the wall of an adjustable smooth rectangular constriction, which is placed at a distance of $30H$ downstream of the entrance. The sensor can be illuminated from the top, the bottom and through the side walls, and the viewing direction is from below. In some of the experiments, a cylinder was placed upstream of the sensor to generate a defined flow disturbance.

4.2 Recording

The illumination and quality of the images of the pillar tips is one of the crucial parameters defining the resolution limit of the wall shear stress measurements. The first experiments show an immediate wash-off of the gold on the pillar heads, causing a strong reduction of the reflectivity during the first use in the flow channel. As mentioned in the Conclusion and outlook section, this problem could be solved for the most recent generation of sensor films. Another effective imaging is achieved when the pillar heads are illuminated by parallel light from the back of the transparent sensor film and are viewed directly onto the tips of the pillars. Hence, the fact is used that the transparent pillars act as optical fibres. The light is transmitted due to the total internal reflection through the pillar to the rounded tip, where it

appears as a small bright spot, which is recorded by the imaging sensor. In contrast to the pillar tip, the base is seen as a larger dark circular area (Fig. 8 right).

For time-resolved imaging of the spatial displacements of the pillar heads, we used a CMOS high-speed camera (Vosskühler HCC1000, frame rate 492 frames/sec at 1024×1024 pixel, pixel size 10×10 microns) equipped with a telecentric microscopic lens with a magnification $M = 10$ and an aperture of 0.4 (Sill Optics). The telecentric lens has two important features; first, it ensures a constant magnification over a certain depth of focus, e.g. approximately 100 microns, and second, the large working distance of 54 mm, which allows to focus onto the sensor at different positions of the adjustable nozzle. The diffraction-limited spot size of the microscope lens is on the order of 30 microns (compare to the equations given by Meinhart and Wereley 2003) and the resolution power is on the order of 1 micron. Other than in microPIV, the resolution limit and, therefore, the accuracy of the measurements in this imaging method is solely given by the resolution power of the lens, since the bright spots of the pillar tips do not overlap in the image plane.

4.3 Image processing and evaluation

The motion of the pillar tips in the flow is achieved in two successive steps. We start by determining the pillar base centre positions to correct any camera or channel vibrations. These coordinates are obtained using the circular Hough transformation and the a priori knowledge of the geometric image diameter of the base. The original images are filtered first using a median filter with a large radius to remove the centre spot; thereafter, the images are inverted and, finally, the so called "canny" filter operator is applied to detect the circular edges of the pillar bases (Fig. 9). Then, the image is subdivided into small interrogation windows centred on a first estimate of the pillar coordinates. The circular Hough


Fig. 7 *Left* sketch of the test flow channel. *Right* bottom view into the contraction zone with the sensor film and the cylinder upstream. The flow is from right to left
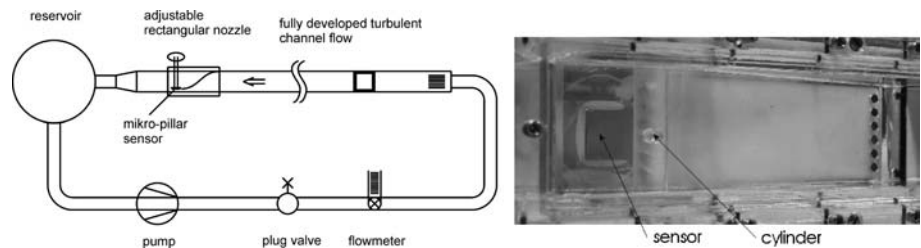
Fig. 8 Images of the different sensors in flow. *Left* pillars of type "A" with sidewise illumination and tip reflection. *Right* pillars of type "B" with backlight illumination
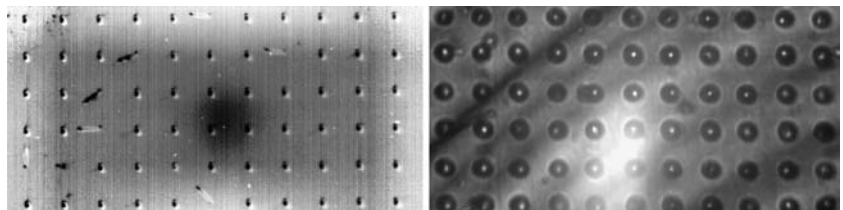
Fig. 9 Image processing steps to determine the pillar base position

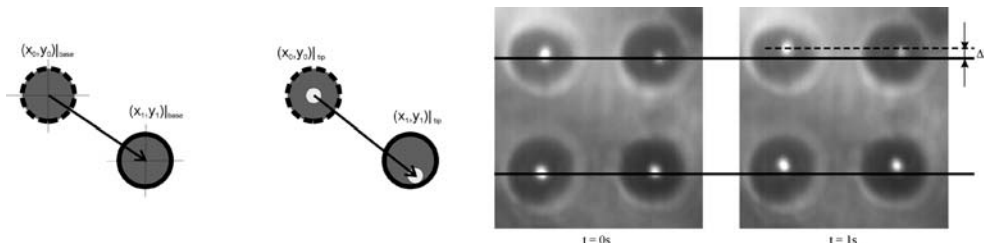original sub-window   median (13 pixel)   canny filter   circular Hough transform
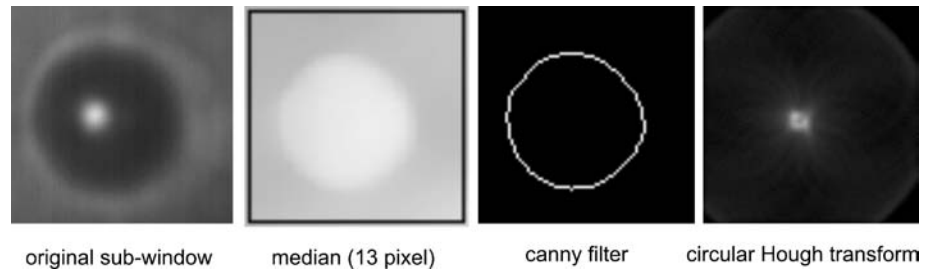
transformation is applied to each interrogation window containing the edges of each single pillar base. The result of the Hough transformation is correlated with a 2D Gaussian function and the maximum in the correlation plane is determined using a 2D Gaussian fit. This provides the coordinates for all pillar bases with subpixel accuracy. The average of all data is used to correct for the overall sensor film motion due to unavoidable channel vibrations (Fig. 10).

In the second step, a cross-correlation method with a Gaussian template mask is applied to determine the centre position of the bright spots on the pillar tips with subpixel accuracy on the order of 1/10th pixel. This results in a detection limit of about 100 nm of the deflection of the pillar tip. The resolution limit of the measurements can be estimated from measurements of the pillars at zero flow with artificially induced channel vibrations. For the given recording conditions, a mean rms value of 0.15 pixels was obtained. This includes the inaccuracy in the determination of both the pillar base position and the pillar tip position.

5 Results and discussion

The first experiments were carried out using coal oil to obtain a larger deflection of the pillars. For these conditions, the flow is almost laminar. Because of the rapid wash-off of the gold on the pillar heads, a strong reduction of the reflectivity occurred that made the optical detection of the smaller pillars with the high-speed camera difficult. This difficulty is even increased

by the low sensitivity of the camera and high required light power. In the case of the smaller pillars, the recording frequency was, therefore, reduced from 492 fps down to 50 fps to increase the visibility of the pillar tips. Figure 11, left displays the streamwise deflection w_x of the pillars of type "A" after the sudden start of the flow. As the flow approaches a constant value for frame number 40, the maximum value of the pillar deflection reaches values of approximately $w_x \approx 12$ μm. Accidentally, a small air bubble was trapped below the sensor, which helped to indicate the fluid motion. As evidenced in Fig. 11 right, the bubble accelerates and moves smoothly around the pillars as the boundary layer develops. At the end of the displayed sequence (frame number 27), it reaches a velocity of 10 mm/s. This corresponds to a w_x equal to half the value of maximum deflection in the impulsive flow step. The profile displayed in Fig. 11 left indicates the first fluid motion at frame number 21, which demonstrates the high sensitivity of the sensor. In addition, the travelling of the bubble around the pillars shows the smooth and approximately for/aft-symmetric flow around the pillars, as expected for creeping flow past a cylinder. Like the presentation in Fig. 11 left, Fig. 12 displays the streamwise deflection w_x of the pillars of type "B" after the sudden start of the flow. The high-speed camera recorded with a rate of 492 fps and only each third measurement point is shown. The circles represent the unfiltered raw data of each image, separated in the streamwise (Fig. 12 left) and the spanwise deflection (Fig. 12 right). Figure 12 demonstrates the high temporal resolution that can be obtained. The small fluctuations in Fig. 12 are correlated with the overall motion of the sensor film. The final pillar deflection values of about 4 μm for the pillars of type "B" are a factor of 3 smaller than those obtained for the smaller pillars of type "A". This tendency is also predicted by Eq. 3. It emphasises the importance of small diameters and high aspect ratios to obtain the highest resolution.

Fig. 10 *Left* correction for the overall camera and channel vibration using the images of the pillar base at rest (x_0, y_0) and with flow (x_1, y_1) and determination of the pillar tip position. *Right* motion-corrected images of the pillars for flow at rest and after the start of the flow in a selected area. The flow direction is from bottom to top
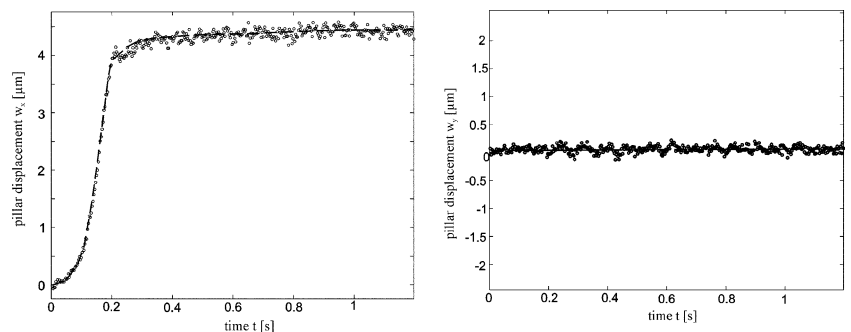
472

Fig. 11 *Left* temporal profile of average pillar displacement after the sudden start of the flow (pillar type "A", frame rate 50 fps, magnification $M=10$). *Right* motion of a small air bubble trapped in the sensor film after the sudden start of the flow. The flow direction is from bottom to top
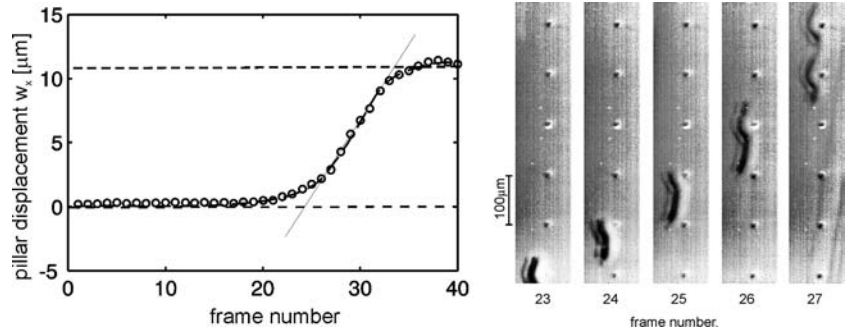
6 Conclusion and outlook

The preliminary results show the feasibility of the presented wall shear imaging sensor concept to measure the wall shear stress in time and on surfaces with high accuracy and high resolution. The described manufacturing techniques allowed to fabricate micropillars with a diameter of approximately 8 µm and a height of 60 µm. An alternative method has been developed which has the potential to fabricate large flexible sensor films. In addition, the new techniques allow the fabrication of pillars with an aspect ratio as high as $L/D=20$, as recently investigated by Schmitz et al. (2005), which leads to sensor films with a sensitivity of up to values of $X\approx100$ µm/Pa. In addition, the usage of polydimethylsiloxane (PDMS) over a wide temperature range and with very high notch impact strength gives the new sensor a unique potential in experimental aerodynamics. Furthermore, the transparency of the micropillars has been used to illuminate and visualise the pillar tips. The micropillars act as microoptical fibres in which the total internal reflection ensures that the light is transmitted to the tip. This fact may also be used as part of an optical readout sensor principle. Overall, the results demonstrate a sufficiently high spatial and temporal resolution of the wall shear stress such that the method can be used for future studies in turbulent boundary layer flows. Ongoing measuring campaigns are underway with the recently fabricated sensor for a transitional boundary layer flow on a flat plate in a large oil channel and in air flows.

Appendix 1

Stokes' drag force in an oscillating boundary layer flow

Unlike Oseen's approximate quasi-steady solution, Stokes' solution for a cylinder oscillating in a fluid accounts for oscillatory flow conditions and added mass effects. The drag force per unit length on the cylinder oscillating with velocity $U(t)=U_0\sin(\omega t)$ is:

$$f_S = |Z_S| \cdot U_0 \sin(\omega t + \zeta_S) \qquad (6)$$

The quantity Z_S is the Stokes' mechanical impedance and ζ_S is a phase shift, both of which are expressed by the following formulae:

$$Z_S = Z_R + iZ_I$$
$$= 4\pi\eta \cdot \frac{-g}{g^2+(\pi/4)^2} + i4\pi\eta \cdot \left[\frac{\omega D^2}{16v} + \frac{\pi/4}{g^2+(\pi/4)^2}\right] \qquad (7)$$

$$|Z_S| = \sqrt{Z_R^2 + Z_I^2}, \qquad (8)$$

$$\zeta_S = \tan^{-1}(Z_I/Z_R) \qquad (9)$$

$$g = 0.577 + \ln\left(\sqrt{\omega D^2/16v}\right) \qquad (10)$$

Fig. 12 Temporal profile of the pillar displacement after the sudden start of the flow (pillar type "B", frame rate 492 fps, magnification $M=10$); *left* streamwise component, *right* spanwise component

To take into account the velocity profile in the boundary layer of the sensor film, we use Stokes' solution for the boundary layer of an oscillating flow with $U(t) = U_0 \sin(\omega t)$ at infinity above a flat plate yielding the following velocity profile:

$$u(z,t) = U(z) \sin\left(\omega t + \xi_S(z)\right) \qquad (11)$$

with:

$$U(z) = U_0 \sqrt{\left(1 - e^{-\beta z} \cdot \cos\left(\beta z\right)\right)^2 + \left(e^{-\beta z} \cdot \sin\left(\beta z\right)\right)^2} \qquad (12)$$

$$\xi(z) = \tan^{-1}\left[e^{-\beta z} \sin\left(\beta z\right) / \left(1 - e^{-\beta z} \cos\left(\beta z\right)\right)\right] \qquad (13)$$

$$\beta = \sqrt{\omega/2v} \qquad (14)$$

The actual force distribution on the pillars in the boundary layer is defined by the relative velocity $u(z,t) - \partial w/\partial t$, leading to the following expression of the force:

$$f_S(z,t) = |Z_s(z)| \big\{ U(z) \sin\left(\omega t + \xi_s(z) + \zeta_s(z)\right) \\ - \dot{w}(z, (t + \zeta_s(z)/\omega)) \big\} \qquad (15)$$

Appendix 2

Frequency response of the pillars in the boundary layer

The response of the pillars to a certain oscillating force $F(z, t)$, which is due to the viscous drag of the fluid moving around the pillars, is described by the one-dimensional Euler–Bernoulli differential equation. Following elastic theory, the governing equation (GE) of the motion of a uniform, homogeneous, one-side clamped cantilever beam with density ρ, cross-sectional area $\tilde{A}$, Young's modulus E and area moment of inertia I is given by:

$$EI \frac{\partial^4 w(z,t)}{\partial z^4} + \rho\tilde{A} \frac{\partial^2 w(z,t)}{\partial t^2} = f_S(z,t) \qquad (16)$$

The damping and added mass effects are included in the drag force $f_S(z, t)$, which is described by the Stokes' solution, see Eq. 15. For the above defined cantilever beam, the necessary boundary conditions to solve Eq. 16 are $w|_{(z=0,t)} = 0$, $\partial w/\partial z|_{(z=0,\ t)} = 0$ for the clamped end at $z = 0$ and $\partial^2 w/\partial z^2|_{(z=L,\ t)} = 0$, $\partial^3 w/\partial z^3|_{(z=L,\ t)} = 0$ for the free end.

For the frequency response in the form of transverse vibrations, we assume a synchronous motion, which implies that the solution $w(z, t)$ is separable in its spatial and temporal components. A particular solution of separated variables in t and z, i.e. the mode vibration $\eta(t)$ and the mode shape $\Phi(z)$, is chosen as given in Eq. 17. It can be shown that the general solution can be expressed as a summation of all particular solutions:

$$w_i(z,t) = \eta_i(t)\, \Phi_i(z) \rightarrow w(z,t) = \sum_{i=1}^{\infty} \eta_i(t)\Phi_i(z) \qquad (17)$$

This solution procedure for Eq. 16 is called the normal mode expansion, in which the modes, i.e. the eigenfunctions, are obtained from the associated eigenvalue problem, i.e. the non-forced case. Then, Eq. 16 can be split into two equations for the time-dependent part $\eta_i(t)$ and for the spatial dependence $\Phi_i(z)$:

$$\text{non - forced: } \ddot{\eta}_i + \underbrace{\left(\frac{EI\Phi_{izzzz}}{\rho\tilde{A}\Phi_i}\right)}_{\text{const}=\omega_i^2}\eta_i = 0$$

$$\text{forced: } \ddot{\eta}_i + \omega_i^2\eta_i = \tilde{C}_i \int\limits_0^L f(z,t)\Phi_i(z)\,\mathrm{d}z$$

$$\text{with } \tilde{C}_i = \left(\rho\tilde{A} \int\limits_0^L \Phi_i^2(z)\mathrm{d}z\right)^{-1} \qquad (18)$$

$$\Phi_{izzzz} - \frac{\rho\tilde{A}}{EI}\omega_i^2\Phi_i = 0 \qquad (19)$$

The mode shapes $\Phi_i(z)$ are independent of the force approximation and can be determined from the non-forced case $f(z, t) = 0$. Under the above constraints, the resulting mode shapes are determined (Volterra and Zachmanoglou 1965):

$$\Phi_i(z) = \frac{1}{2}\left\{ \cos\left(\frac{\lambda_i z}{L}\right) - \cosh\left(\frac{\lambda_i z}{L}\right) \\ + \bar{C}_i\left[\sin\left(\frac{\lambda_i z}{L}\right) - \sinh\left(\frac{\lambda_i z}{L}\right)\right]\right\} \qquad (20)$$

where λ_i and $\bar{C}_i$ are integration constants determined from the boundary conditions. Note that only the first few modes of vibration have significantly large amplitudes. In a first approximation, only the first mode $\Phi_1(z)$ is considered with $\lambda_1 = 1.875$ and $\bar{C}_1 = 0.734$. In addition, since the system is analysed for the steady-state response, we assume a response with the same frequency dependence as the force in the form:

$$U(t) = U_0 \sin\left(\omega t\right) \rightarrow \eta_1(t) = H_1 \sin\left(\omega t + \varphi_1\right) \qquad (21)$$

Plugging the expression of the force given in Eq. 15 and the mode vibration given by Eq. 21 into Eq. 18, together with the first mode shape in Eq. 20, one obtains the following analytical expression for the amplitude H_1 and phase ϕ_1 of $\eta_1(t)$:

$$H_1 = \sqrt{\frac{A_1^2 + B_1^2}{\left(\omega_1^2 - \omega^2 - \omega C_1\right)^2 + \omega^2 D_1^2}} \qquad (22)$$

$$\varphi_1 = \tan^{-1}\left(\frac{(\omega_1^2 - \omega^2 - \omega C_1)B_1 - \omega D_1 A_1}{(\omega_1^2 - \omega^2 - \omega C_1)B_1 + \omega D_1 A_1}\right) \tag{23}$$

with:

$$A_1 = \tilde{C}_1 \int_0^L |Z_S(z)|U(z)\Phi_1(z)\cos\left(\zeta_S(z) + \xi_S(z)\right)\mathrm{d}z \tag{24}$$

$$B_1 = \tilde{C}_1 \int_0^L |Z_S(z)|U(z)\Phi_1(z)\sin\left(\zeta_S(z) + \xi_S(z)\right)\mathrm{d}z \tag{25}$$

$$C_1 = \tilde{C}_1 \int_0^L |Z_S(z)|\Phi_1^2(z)\sin\left(\zeta_S(z)\right)\mathrm{d}z \tag{26}$$

$$D_1 = \tilde{C}_1 \int_0^L |Z_S(z)|\Phi_1^2(z)\cos\left(\zeta_S(z)\right)\mathrm{d}z \tag{27}$$

Finally, the deflection of the first-mode vibration of the beam in a steady-state response is given as:

$$w_1(z,t) = \eta_1(t)\Phi_1(z) = H_1 \sin\left(\omega t + \varphi_1\right)\Phi_1(z) \tag{28}$$

and the tip deflection amplitude reads as:

$$w_L = H_1 \Phi_1(L) \tag{29}$$

References

Bernard PS, Wallace JM (2002) Turbulent flow: analysis, measurement, and prediction. Wiley, New York

Brücker C, Spatz J, Schröder W (2004) Wall shear stress imaging in turbulent flows using microstructured surfaces with flexible micropillars. In: Proceedings of the 10th EUROMECH European turbulence conference (ETC 10), The Norwegian University of Science and Technology, Trondheim, Norway, 29 June–2 July 2004

Chen J, Fan Z, Zou J, Engel J, Liu C (2003) Two-dimensional micromachined flow sensor array for fluid mechanical studies. J Aerospace Eng 16(2):85–97

Czarske J, Büttner L, Razik T, Welling H (2001) Measurement of velocity gradients in boundary layers by a spatially resolving laser Doppler sensor. In: Proceedings of the SPIE's annual meeting, conference 4448, optical diagnostics for fluids, solids, and combustion session micro optics, 29–31 July 2001, San Diego, California

Fernholz HH, Janke G, Schrober M, Wagner PM, Warnack D (1996) New developments and applications of skin-friction measuring techniques. Meas Sci Technol 7:1396–1409

Gharib M, Modarress D, Fourguette D, Wilson D (2002) Optical microsensors for fluid flow diagnostics. In: Proceedings of the 40th AIAA Aerospace sciences meeting and exhibit. Reno, Nevada, January 2002

Gibson A, Chernoray V, Löfdahl L (2004) Time-resolved wall shear stress measurements using MEMS. In: Proceedings of the XXI international congress of theoretical and applied mechanics (ICTAM 2004), Warsaw, Poland, 15–21 August 2004

Glassmaker NJ, Jagota A, Hui CY, Kim J (2004) Design of biomimetic fibrillar interfaces: 1. making contact. J R Soc Lond Interface 1:23–33

Khoo BC, Durst F (2002) Near wall measurements with hot-wires and hot-film probes require special care. Dantec Dynamics News, vol 9 no 4, available at http://www.dantecdynamics.com/applications/Fundamental%20Fluid/cta_Near%20wall%20measurements/

Löfdahl L, Gad-el-Hak M (1999) MEMS application in turbulence and flow control. Prog Aerospace Sci 35:101–203

Lötters JC, Olthuis W, Veltink PH, Bergveld P (1997) The mechanical properties of the rubber elastic polymer polydimethylsiloxane for sensor applications. J Micromech Microeng 7:145–147

Meinhart CD, Wereley ST (2003) The theory of diffraction-limited resolution in microparticle image velocimetry. Meas Sci Technol 14:1047–1053

Naughtona JW, Sheplak M (2002) Modern developments in shear-stress measurement. Prog Aerospace Sci 38:515–570

Osaki Y, Ohyama T, Yasuda T, Shimoyama I (2000) An air flow sensor modelled on wind receptor hairs of insects. In: Proceedings of the 13th annual international conference on micro electro mechanical systems (MEMS 2000), Miyazaki, Japan, January 2000, pp 531–536

O'Sullivan S, Nagle R, McEwen JA, Casey V (2003) Elastomer rubbers as deflection elements in pressure sensors: investigation of properties using a custom designed programmable elastomer test rig. J Phys D: Appl Phys 36:1910–1916

von Papen T, Buder U, Ngo HD, Obermeier E (2002) High resolution wall shear measurement using a MEMS surface fence sensor. In: Proceedings of the 16the European conference on solid-state transducers (Eurosensors XVI), 15–18 September 2002, Prague, Czech Republic, pp 744–747

Roos W, Roth A, Konle J, Presting H, Sackmann E, Spatz J (2003) Freely suspended actin cortex models on arrays of microfabricated pillars. Chem Phys Chem 4:872–876

Roy P, Rajfur Z, Pomorski P, Jacobson K (2002) Microscope-based techniques to study cell adhesion and migration. Nat Cell Biol 4(4):E91–E96

Rudko O (2001) Design of a low-frequency sound sensor inspired by insect sensory hairs. Masters thesis, Binghamton University, New York

Schmitz GJ, Brücker Ch, Jacobs P (2005) Manufacture of high-aspect ratio micro-hair sensor arrays. J Micromech Microeng (in press)

Shimozawa T, Kumagai T, Baba Y (1998) Structural scaling and functional design of the cercal wind-receptor hairs of cricket. J Comp Physiol A 183:171–186

Sturzebecher D, Anders S, Nitsche W (2001) The surface hot-wire as a means of measuring mean and fluctuating wall shear stresses. Exp Fluids 31(3):294–301

Timoshenko SP, Gere JM (1961) Theory of elastic instability, 2nd edn. McGraw-Hill, New York

van Baar JJ, Dijkstro M, Wiegerink RJ, Lammerink TSJ, Kijnen (2003) Fabrication of arrays of artificial hairs for complex flow pattern recognition. In Proceedings of the 2nd IEEE international conference on sensors, Toronto, Canada, October 2003, pp 22–24

Venier P, Maggs AC, Carlier MF, Pantaloni D (1994) Analysis of microtubule rigidity using hydrodynamic flow and thermal fluctuations. J Biol Chem 269:13353–13360

Volterra E, Zachmanoglou EC (1965) Dynamics of vibrations. Charles E. Merrill Books, Columbus, Ohio

Weeks B, Camarero J, Noy A, Miller A, Stanker L, De Joreo J (2003) A micro cantilever-based pathogen detector. In: Proceedings of the 2003 nanotechnology conference and trade show (Nanotech 2003), San Francisco, California, 23–27 February 2003